Self-aggregation of clouds in conditionally unstable moist convection

Olivier Pauluis[a,1] and Jörg Schumacher[b]

[a]Courant Institute of Mathematical Sciences, New York University, 251 Mercer Street, New York, NY 10012-1185; and [b]Institute of Thermodynamics and Fluid Mechanics, Technische Universität Ilmenau, P.O. Box 100565, D-98684 Ilmenau, Germany

Edited* by Katepalli R. Sreenivasan, New York University, New York, NY, and approved June 13, 2011 (received for review February 10, 2011)

The behavior of moist Rayleigh–Bénard convection is investigated using a Boussinesq model with a simplified thermodynamics for phase transitions. This idealized configuration makes the problem accessible to high-resolution three-dimensional direct numerical simulations without small-scale parameterizations of the turbulence for extended layers with aspect ratios up to 64. Our study is focused on the frequently observed conditionally unstable environment that is stably stratified for unsaturated air, but is unstable for cloudy air. We find that no sharp threshold for the transition to convective turbulence exists, a situation similar to wall-bounded shear flows. Rather, the transition depends on the amplitude of the initial perturbation of the quiescent equilibrium and on the aspect ratio of the convective domain. In contrast to the classical dry Rayleigh–Bénard case, convection is highly asymmetric with respect to the vertical direction. Moist upwelling air inside turbulent cloud aggregates is surrounded by ambient regions of slowly descending unsaturated air. It is also found that conditionally unstable moist convection is inefficient at transporting energy. Our study suggests that there is an upper bound on the Nusselt number in moist convection that is lower than that of the classical dry case.

Convective processes in the Earth's atmosphere are often associated with condensation of water vapor and the formation of clouds. These involve spatial scales as small as a micron for the activation of cloud water droplets and as large as a few kilometers for a whole cloud, with time scales ranging from milliseconds to hours (1, 2). Convective systems are often themselves embedded within larger structures, such as mesoscale cloud clusters or midlatitude baroclinic eddies. Because of their complex multiscale physics, clouds remain one of the main sources of uncertainty in predictions of future climate change (3, 4). This holds particularly true for low clouds over subtropical and tropical oceans (5), where small changes in cloud behavior can dramatically alter the amount of solar energy absorbed or reflected. Even with state-of-the-art large eddy simulations that can describe the dynamics on mesoscales in atmospheric layers with a side length of up to approximately 10^2 km and grid resolutions of 100 m or less, many of the dynamically relevant scales still remain unresolved and have to be parameterized (6). Our understanding of the formation of clouds, their life cycles, and the resulting turbulent transport is still incomplete. Further progress can be gained by increasing the resolution of the numerical model (7, 8) and a refinement of the subgrid scale parameterizations to obtain the most realistic simulations of convection. Equally important for our understanding is the need to disentangle the various phenomena and to identify the most important physical processes that determine the dynamics of clouds in the atmosphere. This is the approach followed in this paper in which we analyze the behavior of convection in an idealized set of equations that reproduces the formation and structure of clouds and cloud clusters.

The present study is based on a model of moist turbulent convection with a simplified thermodynamics of cloudy air. It is closely related to the classical Rayleigh–Bénard problem, but includes phase transitions between the gaseous and liquid phase and the effect of latent heat release on the buoyancy of air parcels. In practice, phase transition results in a discontinuity of partial derivatives with respect to thermodynamic state variables at the phase boundary (9–11). The advantage of this model is that it becomes readily accessible to mathematical investigation and direct numerical simulations (DNSs) of turbulence. Because all flow scales down to the viscous Kolmogorov scale are resolved, the accessible Rayleigh numbers remain moderate. We demonstrate that this simplified model is not only capable to simulate cloud formation processes, but also indicates that the complex dynamics of moist convection results in the emergence of previously undescribed convective regimes that do not exist in the absence of phase transition.

This study focuses on one particularly important regime, that of a *conditionally unstable* layer, which occurs when the atmosphere is stable for unsaturated parcels, but unstable for saturated parcels. Thus, although unsaturated parcels remain stable with respect to small vertical shifts, saturated moist air parcels can rise up and trigger saturated convective plumes. In a conditionally unstable atmosphere, moist unstable air rises up in narrow columns that are surrounded by wider regions of subsiding unsaturated air, described first by Bjerknes in a strikingly simple model (12), and confirmed later in more detail in a linear stability analysis (9, 13, 14). Our work extends this stability analysis for small perturbations and determines whether the convective plumes can be sustained. In particular, we show that if the aspect ratio of the convection domain is not sufficiently large, convection is suppressed or only present as a recharge–discharge mechanism, with short intense bursts of convection separated by long quiescent intervals. At large aspect ratio, however, a statistically stationary convective regime can be sustained, which is characterized by the presence of isolated turbulent cloud aggregates separated by dry regions. The onset of turbulent moist convection is similar to the transition to turbulence in wall-bounded shear flows (15, 16). In particular, we demonstrate, that turbulent moist convection can occur in a subcritical regime. However, in such case, the transition to turbulence has no sharp transition threshold, but rather depends on the aspect ratio of the domain and the amplitude of the initial perturbation.

Moist turbulence under conditional instability differs significantly from classical dry Rayleigh–Bénard convection. In particular, transport of heat across the layer is found to be highly asymmetric with a broken upside-down symmetry for buoyancy flux and other quantities that are not invariant with respect to adiabatic phase changes. Furthermore, we postulate here, in contrast to the classic Rayleigh–Bénard problem, the existence of an upper bound on the Nusselt number that is finite for all Rayleigh numbers resulting from the stabilization through the subsidence of warm, dry air in the environment.

Author contributions: O.P. and J.S. designed research, performed research, analyzed data, and wrote the paper.

The authors declare no conflict of interest.

*This Direct Submission article had a prearranged editor.

[1]To whom correspondence should be addressed. E-mail: pauluis@cims.nyu.edu.

This article contains supporting information online at www.pnas.org/lookup/suppl/doi:10.1073/pnas.1102339108/-/DCSupplemental.

Conditionally Unstable Moist Convection

We solve the three-dimensional Boussinesq–Navier–Stokes equations in a rectangular domain of horizontal size L and height H for aspect ratios $A = L/H$ between 4 and 64 by a standard pseudospectral method (11, 17, 18). The equations are given by

$$\partial_t \mathbf{u} + (\mathbf{u}\cdot\nabla)\mathbf{u} + \nabla p = \nu\nabla^2\mathbf{u} + B(D,M,z)\mathbf{e}_z, \quad [1]$$

$$\nabla\cdot\mathbf{u} = 0, \quad [2]$$

$$\partial_t D' + (\mathbf{u}\cdot\nabla)D' = \kappa\nabla^2 D' + G_D u_z, \quad [3]$$

$$\partial_t M' + (\mathbf{u}\cdot\nabla)M' = \kappa\nabla^2 M' + G_M u_z, \quad [4]$$

Here, $\mathbf{u}$ is the velocity field, p is the kinematic pressure, ν is the kinematic viscosity, and κ is the scalar diffusivity. Two prognostic fields—a *dry* buoyancy D and a *moist* buoyancy M—are decomposed into linear profiles across the layer, $\bar{D}(z)$ and $\bar{M}(z)$, plus deviations, D' and M'. $G_D = (D_0 - D_H)/H$ and $G_M = (M_0 - M_H)/H$. The fields D and M are linear combinations of the total water content (cloud water droplets plus vapor) and the potential temperature on the unsaturated and saturated side of the phase boundary (11). The dry buoyancy field D is thus proportional to the liquid water potential temperature and the moist buoyancy field M to the equivalent potential temperature. We apply free-slip boundary conditions for the flow at $z = 0$ and $z = H$ and prescribe both buoyancies to D_0, M_0 and D_H, M_H, respectively. The buoyancy field B follows to

$$B(\mathbf{x},t) = \max(M(\mathbf{x},t), D(\mathbf{x},t) - N_s^2 z), \quad [5]$$

with the fixed Brunt–Vaisala frequency N_s that is determined by the moist adiabatic lapse rate (11). Eq. **5** is the saturation condition that determines if liquid water and thus clouds are formed in the layer. Clouds are defined as those space–time points in which the liquid water content q_l is positive. It is given by the condition $M > D - N_s^2 z$ in our model.

The flow is characterized by five nondimensional numbers: the Prandtl number, the dry Rayleigh number, the moist Rayleigh number, which are given by

$$Pr = \frac{\nu}{\kappa}, \quad [6]$$

$$Ra_D = \frac{(D_0 - D_H)H^3}{\nu\kappa}, \quad [7]$$

$$Ra_M = \frac{(M_0 - M_H)H^3}{\nu\kappa}, \quad [8]$$

and two additional parameters tied to the expression (**5**) for the buoyancy. They quantify the liquid water content at the bottom and top boundary planes

$$CW_0 = \frac{M_0 - D_0}{N_s^2 H}, \qquad CW_H = 1 + \frac{M_H - D_H}{N_s^2 H}. \quad [9]$$

Here, we consider atmospheric convection over the ocean, which implies $Pr = 0.7$ and that the lower boundary is at saturation; i.e., $CW_0 = 0$. Conditional instability occurs when the atmosphere is stably stratified for unsaturated parcels, but saturated parcels are convectively unstable, which translates to $Ra_M > 0$ and $Ra_D < 0$.

The amplitudes of both buoyancy fields at the top and bottom planes determine the amount of potential energy that can be converted into fluid motion. The convectively available potential energy (CAPE) (10) for a parcel rising from the surface $z = 0$ is given by

$$\mathrm{CAPE} = -\int_0^H [B(\bar{D}(z),\bar{M}(z),z) - B(D_0,M_0,z)]\mathrm{d}z. \quad [10]$$

A necessary condition for the onset of convection is CAPE > 0. For the case $D_0 = M_0 = 0$ and $M_H < 0$, a positive value of CAPE requires $D_H < N_s^2 H$. We can assign this absolute stability threshold with a so-called *Brunt–Vaisala Rayleigh number*

$$Ra_{\mathrm{BV}} = \frac{N_s^2 H^4}{\nu\kappa} \quad [11]$$

so that the convection layer is absolutely stable for $Ra_D \le -Ra_{\mathrm{BV}}$.

A positive value of CAPE is, however, not sufficient to guarantee unstable convective motions. The linear stability of the equilibrium solutions is illustrated in Fig. 1 *A–C*. If the quiescent equilibrium state is unsaturated, i.e.,

$$-N_s^2 z < \bar{M}(z) < \bar{D}(z) - N_s^2 z, \quad [12]$$

as indicated in Fig. 1*A*, small perturbations cannot cause a transition to convection, despite positive CAPE. We refer to this case as *subcritical conditionally unstable equilibrium*, which corresponds to $-Ra_{\mathrm{BV}} < Ra_D < Ra_M - Ra_{\mathrm{BV}}$. In Fig. 1*B*, the stable stratification of D is decreased to a degree that the equilibrium is exactly at the onset of saturation, i.e.,

$$\bar{M}(z) = \bar{D}(z) - N_s^2 z, \quad [13]$$

or $CW_0 = CW_H = 0$. We refer to this equilibrium state as the *Kuo–Bretherton (KB) regime* (9, 13, 14). It corresponds to a dry Rayleigh number, which is given by

$$Ra_D^{\mathrm{KB}} = Ra_M - Ra_{\mathrm{BV}}. \quad [14]$$

Finally, if

$$\bar{M}(z) > \bar{D}(z) - N_s^2 z, \quad [15]$$

which corresponds to $Ra_M - Ra_{\mathrm{BV}} \le Ra_D \le 0$, the equilibrium state is saturated and is linearly unstable as long as the moist Rayleigh number is larger than the classical value of $Ra_c = 27\pi^4/4$ for free-slip boundaries (10). This configuration is referred to here as *supercritical conditionally unstable equilibrium*.

Fig. 1*D* summarizes our parametric studies of the onset of moist convection for $Ra_M = 3.73 \times 10^5$ and $CW_0 = 0$. For the supercritical regime, $Ra_D > Ra_D^{\mathrm{KB}}$ (or $Ra_D/Ra_D^{\mathrm{KB}} < 1$), we always observe a transition to moist turbulent convection that is accompanied with a closed cloud layer at the top. In contrast, the transition depends sensitively on the aspect ratio of the box for the subcritical regime, $Ra_D < Ra_D^{\mathrm{KB}}$ (or $Ra_D/Ra_D^{\mathrm{KB}} > 1$). Fig. 1*D*, *Inset* demonstrates that for $A = 4$ no transition to convection was detected in this case. It shows that besides the degree of stratification, the onset of convection depends on the aspect ratio of the layer. For larger aspect ratios, a transition of the subcritical equilibrium to moist turbulent convection is then possible as demonstrated in two series of DNSs at aspect ratios $A = 16$ and $A = 32$. Depending on the degree of stratification and for identical initial perturbations, we detect a transition to convective turbulence or not (as indicated by the alternating colors of the asterisks in the plot). The comparison of both series indicates also that an increase of the aspect ratio enhances the probability to initiate moist convection. Furthermore, we found that—similarly to the transition to turbulence in wall-bounded shear flows—

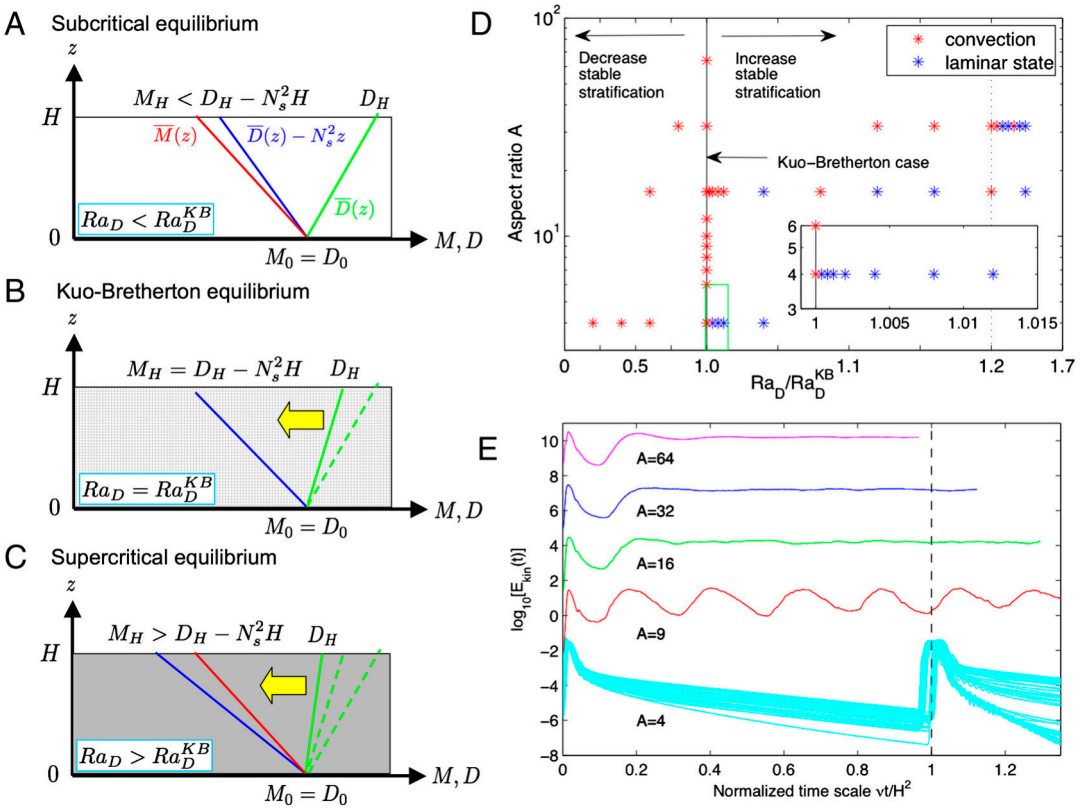

Fig. 1. Transition to convective turbulence in a conditionally unstable moist convection layer. (*A*) Configuration of a fully unsaturated subcritical conditionally unstable equilibrium. (*B*) The Kuo–Bretherton (KB) equilibrium of a conditionally unstable atmosphere. The whole layer is neither saturated nor unsaturated. (*C*) Configuration of a supercritical conditionally unstable equilibrium. The crossover from regime *A* to *C* is obtained by decreasing D_H (or increasing the dimensionless parameter CW_H) and thus the stable stratification of $D(\mathbf{x},t)$. (*D*) Transition to moist convection as a function of aspect ratio and dry Rayleigh number. Each data point is a long-time DNS. Red asterisks indicate a crossover to sustained moist convection. Blue asterisks indicate a return to the initial equilibrium. For all data $CW_0 = 0$, $Pr = 0.7$ and $Ra_M = 3.73 \times 10^5$. The parameter settings result to $Ra_D^{KB} = -1.24 \times 10^5$ and $-Ra_{BV} = 4Ra_D^{KB}$. The *x* axis of the diagram has been stretched by a factor of five between 1 and 1.2 in order to highlight better alternations between return to equilibrium or transition to sustained convection. The fraction of the parameter space, which is indicated as a green box, is magnified (*Inset*) in order to demonstrate the absence of transition in the subcritical regime at small aspect ratios. (*E*) Kinetic energy as a function of time for different aspect ratios in the KB regime. Data for $A = 9$, 16, 32, and 64 have been shifted by multiples of 10^3 for better visibility. The run at $A = 4$ was repeated with 50 different perturbation amplitudes in order to demonstrate the robustness of the recharge–discharge regime.

convection can be sustained in the subcritical regime for a sufficient initial perturbation.

Fig. 1*E* shows the turbulent kinetic energy $E_{\mathrm{kin}}(t) = 1/2V \int_V \mathbf{u}^2 \mathrm{d}V$ as a function of time for five aspect ratios in the KB regime. For the smallest aspect ratio $A = 4$, we observe a highly intermittent on–off convection, with an intense but short-lived outburst of convection followed by a slow decay, until a new convective outburst occurs. The time separating two convective outbursts is approximately given by the diffusion time $t_d = H^2/\nu$. This behavior is robustly reproduced for different amplitudes of the initial perturbation and different Rayleigh number. With increasing aspect ratio, this recharge–discharge cycle is replaced by a sustained moist turbulent convective regime that is first pulsating ($A = 9$) before turning to the statistically stationary turbulent case at larger domains. The latter cases will be discussed in the following.

Self-Aggregation of Clouds

The structure and statistical properties of moist convection in a conditionally unstable layer differ significantly from classical dry turbulent Rayleigh–Bénard convection (19). Fig. 2 plots instantaneous top views on the layer for different aspect ratios. Filled contours correspond with the moist buoyancy field. In addition, the figures show the cloud boundary as a transparent three-dimensional isosurface. It can be seen that the convection (and thus the clouds) are organized in localized turbulent aggregates

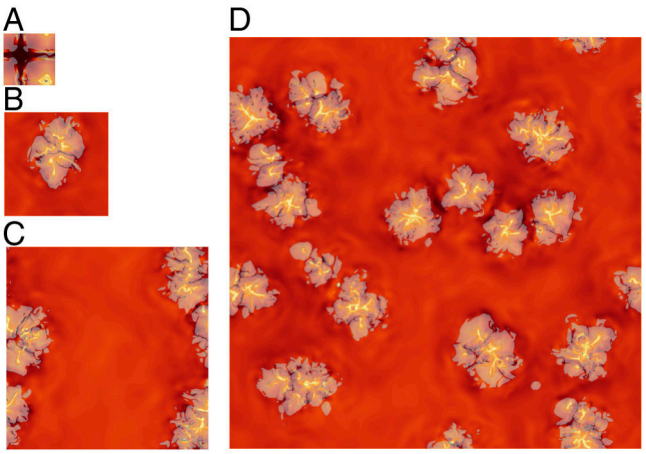

Fig. 2. Top view on instantaneous cloud patterns in the Kuo–Bretherton case for different aspect ratios. The plots in the figure display contours of the moist buoyancy field $M_0 \geq M \geq M_H$ in the midplane overlaid by the three-dimensional cloud boundary $q_l(\mathbf{x},t) = M(\mathbf{x},t) - (D(\mathbf{x},t) - N_s^2 z) = 0$ as a transparent isosurface. For all shown data $CW_0 = 0$, $Pr = 0.7$, $Ra_M = 3.73 \times 10^5$, and $Ra_D^{KB} = -1.24 \times 10^5$. (*A*) $A = 8$ with a grid resolution $512 \times 512 \times 65$ points. (*B*) $A = 16$ with a grid resolution $1{,}024 \times 1{,}024 \times 65$ points in the DNS. *C* is for $A = 32$ with a computational grid of $2{,}048 \times 2{,}048 \times 65$ points. *D* is for $A = 64$ with $4{,}096 \times 4{,}096 \times 65$ points in the simulation. The grid resolution is thus unchanged.

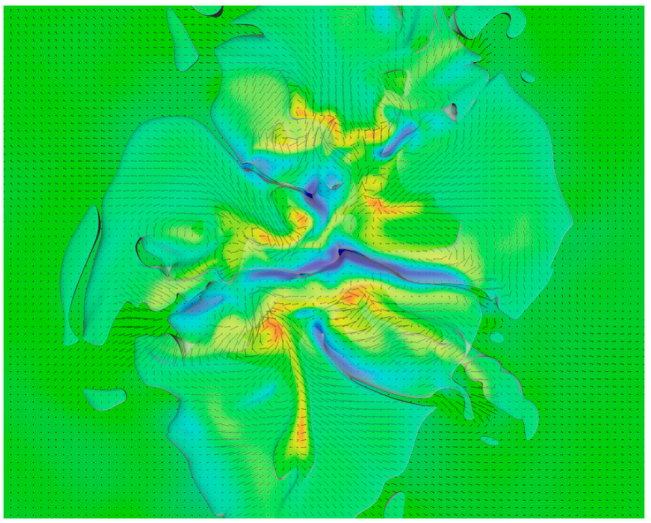

Fig. 3. Top view into a localized turbulent cloud aggregate for $A = 16$. The vector plot of the horizontal velocity components in the midplane of the layer is shown together with a contour plot of the vertical velocity component (orange, upward directed velocity; blue, downward directed velocity). The transparent isovolume is the cloud boundary.

that are surrounded by ambient unsaturated air. Fig. 3 displays a zoom into such aggregate plotting the cloud boundary and velocity field for $A = 16$. Turbulence is present inside the clouds. For sufficiently large aspect ratio ($A > 16$) more than one localized cloud aggregate can be observed. These configurations are typical for the KB and subcritical regimes. A large-scale organization into traveling clusters of tilted thermal plumes has been observed in experiments of single-phase turbulent convection in water at $Pr = 7$ (20, 21). In the present system, the moist plumes do not move around significantly. Their shape is more similar to turbulent spots in shear flows (15) or to spiral turbulence in Taylor–Couette flow (22).

The self-aggregation of moist convection is characteristic of the conditionally unstable regime and contrasts sharply with a homogeneous cloud layer obtained in simulations of the absolutely unstable regime with positive values for both dry and moist Rayleigh numbers, as discussed in refs. 11, 17, and 18. This difference is illustrated by Figs. S1 and S2, which compare the cloud cover and other statistics between two simulations that differ by the sign of Ra_D having nearly the same Ra_M. The self-aggregated clouds separated by dry, stable regions of the conditionally unstable regime are consistent with the phenomenological model by Bjerknes (12). Localized upward motion of moist air requires broad surrounded regions of *slowly subsiding* dry air in order to close the "loop of convective motion." This in turn explains the observations, summarized in Fig. 1 *D* and *E*, that for the smaller aspect ratios this loop cannot be initiated and thus perturbations of the initial equilibrium decay for $Ra_D/Ra_D^{\mathrm{KB}} > 1$.

Fig. 4*A* shows the cloud cover as we move from the supercritical regime for $Ra_D/Ra_D^{\mathrm{KB}} < 1$ to the subcritical regime $Ra_D/Ra_D^{\mathrm{KB}} > 1$. While in the supercritical regime the whole layer is covered by clouds, the subcritical case is associated with a significant drop below 100%. Fig. 4*A*, *Inset* demonstrates that the cloud cover remains practically unchanged for $A \geq 16$, suggesting that this aspect ratio is appropriate to sustain isolated cloud aggregates at the given Rayleigh number. The kinetic energy as a function of time is shown in Fig. 4*B* for all runs at $A = 32$. We detect either a return to the quiescent equilibrium (corresponding with blue asterisks in Fig. 1*D*) or to sustained turbulence (red asterisks in Fig. 1*D*). All runs were perturbed identically at the beginning. Fig. 4*B*, *Inset* shows that the root-mean-square velocity decreases linearly with increasing stratification. Extrapolating this linear decay to $u_{\mathrm{rms}} = 0$ suggests that no convection is possible for $Ra_D \lesssim 2Ra_D^{\mathrm{KB}}$ at the given parameters, i.e., significantly above the absolute stability threshold $Ra_D = 4Ra_D^{\mathrm{KB}} = -Ra_{\mathrm{BV}}$ in the present setting.

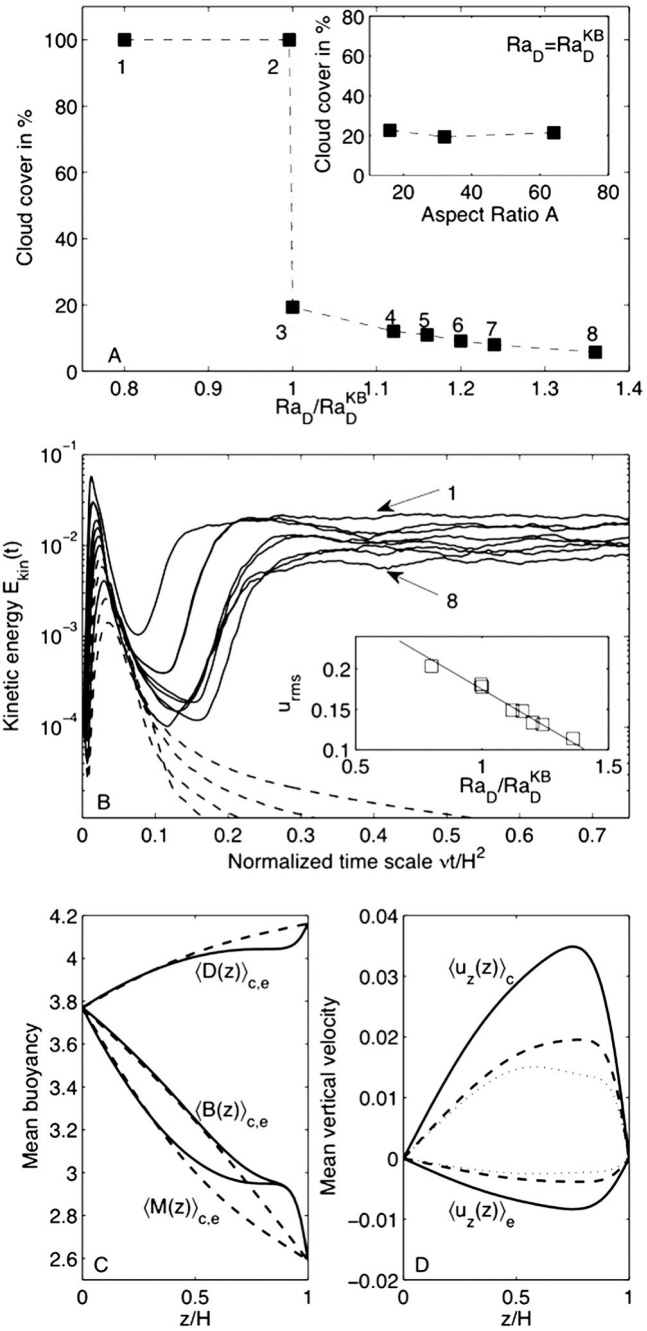

Fig. 4. Cloud cover and turbulent transport inside and outside the cloud aggregates. (*A*) Cloud cover as a function of Ra_D (normalized by Ra_D^{KB}) at $A = 32$. (*Inset*) Comparison of the cloud cover for aspect ratios $A = 16$, 32, and 64 at $Ra_D = Ra_D^{\mathrm{KB}}$. (*B*) Turbulent kinetic energy as a function of time. The numbering corresponds with *A*. (*Inset*) The root-mean-square velocity for the eight turbulent runs of *B*. (*C* and *D*) Plane–time averages inside $\langle\cdot\rangle_c$ and outside $\langle\cdot\rangle_e$ the clouds. Clouds are defined as columns with a liquid water content larger than zero. Data are for $A = 32$. (*C*) Mean vertical profiles of the buoyancy fields *D*, *M*, and *B*. Solid lines are for $\langle\cdot\rangle_c$ and dashed lines are for $\langle\cdot\rangle_e$. (*D*) Vertical mean velocity for $(Ra_M, Ra_D) = (3.73 \times 10^5, -1.24 \times 10^5)$ (solid line), $(1.87 \times 10^6, -6.20 \times 10^5)$ (dashed line), and $(3.73 \times 10^6, -1.24 \times 10^6)$ (dotted line).

both regions for the buoyancy fields. We see that the profiles outside the clouds are very close to the linear equilibrium case. In Fig. 4*D*, the vertical velocity is on average upward inside the cloud and downward outside the cloud, indicating presence of a broader overturning circulation with air rising within the cloudy regions, and subsiding outside. Furthermore, we found that with decreasing diffusivity in the layer, the maximum amplitudes of the mean upward and downward flow decrease. This turns out to be in line with a decreasing cloud cover.

Bound on Convective Transport

One of the intriguing properties of the conditionally unstable moist convection is the low magnitude of the transport as measured by the dimensionless Nusselt number. As convection acts to homogenize the bulk of the layer, it also increases the vertical gradient of the buoyancy in a tiny layer close to the bottom and top planes (10). Right at the free-slip boundaries with $u_z = 0$, the Nusselt number is solely determined by the diffusive transport

$$Nu_D = \frac{H}{D_H}\frac{\partial\langle D\rangle_{A,t}}{\partial z}\bigg|_{z=0}, \qquad [16]$$

with $\langle\cdot\rangle_{A,t}$ being a plane–time average. In order to sustain convection, it is reasonable to assume that air parcels originating from $z = 0$ with $M = D = 0$ should be positively buoyant with respect to the mean buoyancy field $\langle B\rangle_{A,t}$, which requires $\partial\langle B\rangle_{A,t}/\partial z < 0$ at $z = 0$. This requires with Eq. **5** that $\partial\langle D\rangle_{A,t}/\partial z|_{z=0} < N_s^2$. Following the argumentation by Malkus (23) for classical Rayleigh–Bénard convection, we suggest that fully developed moist convection must remain unstable within the boundary layer. This implies that the vertical gradient of D must remain less than the square of the Brunt–Vaisala frequency N_s^2, which yields an upper bound on the Nusselt number given by ($D_0 = 0$)

$$Nu_D < \frac{N_s^2 H}{D_H} = \frac{Ra_{\mathrm{BV}}}{|Ra_D|}. \qquad [17]$$

Fig. 5 shows the Nusselt number obtained in our simulations, which all satisfy the bound. We also show a simulation for which the amplitude of the dry Rayleigh number is exactly the same, but positive and thus not in the conditionally unstable regime. In this case we are practically in the classical convection regime and the bound (Eq. **17**) is immediately exceeded. In addition, we add the rigorous upper bound as derived by Busse (24) and Howard (25).

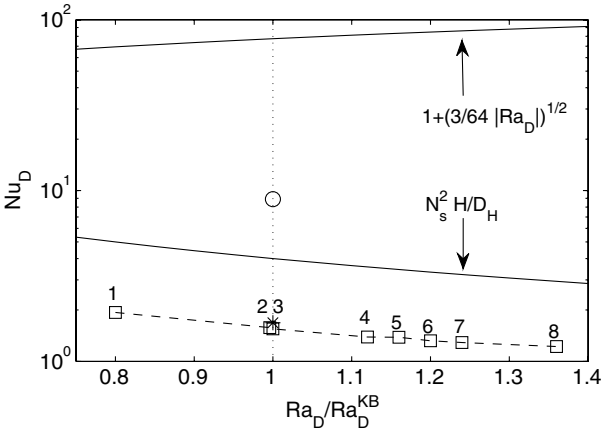

Fig. 5. Nusselt number dependence. Besides the data for the eight runs from Fig. 4, we add the suggested upper bound (lower solid line), the prediction from Howard (25) (upper solid line), which is derived for the no-slip boundary case, but can be expected to be similar for the free-slip case. The asterisk data point is a run at 10 times larger Rayleigh number. The open circle is a run for which the magnitudes of Ra_D and Ra_M agree with run 3, except that both buoyancy fields are unstably stratified; i.e., $Ra_D > 0$. The corresponding initial equilibrium state is fully saturated.

Eq. **17** can be interpreted as resulting from the presence of a diffusive boundary layer of thickness $\delta_D > D_H/N_s^2$. This thickness depends only on the parameter N_s^2, which is proportional to the total amount of water vapor in the air. When diffusivity is decreased, the thickness remains unchanged, and thus the diffusive flux that can be driven across this boundary layer is reduced. This requires a similar decrease in the convective transport, corresponding to convective plumes being confined to a smaller region of the domain. Self-aggregation would require a larger and larger aspect ratio as the diffusivity decreases. This is demonstrated in Fig. 6 where we show typical cloud cover snapshots as a function of the Rayleigh number and the aspect ratio.

Moist convection at high Rayleigh number differs fundamentally from classic Rayleigh–Bénard convection. Indeed, for the latter, Malkus (23) argued that the boundary layer thickness in turbulent convection should follow a power law of the form $Ra^{-1/3}$, corresponding to a Nusselt number proportional to $Ra^{1/3}$. In contrast, the bound (Eq. **17**) is independent of viscosity, so that the Nusselt number remains finite even for very large Rayleigh numbers. This distinction arises from the different stabilization mechanisms. For dry convection, stabilization results from molecular dissipation within a thin boundary layer balancing the buoyancy forcing. In conditionally unstable convection, stabilization occurs when the dry stability becomes sufficiently strong to prevent even the ascent of saturated parcels. This also indicates that although diffusive processes are mostly confined to shallow boundary layers in dry convection, diffusive fluxes remain quite important through a large portion of the atmospheric layer in the case of conditionally unstable Rayleigh–Bénard convection.

Discussion

We have shown here that conditionally unstable moist convection differs from dry Rayleigh–Bénard convection in multiple ways. Stability analysis indicates the existence of subcritical regime that is stable for small amplitude perturbation, but can evolve to a fully turbulent regime for finite amplitude disturbance. This situation is similar to the transition to turbulence in shear flows, which depends on the perturbation amplitude (15). However, in contrast to wall-bounded shear flows, where localized turbulent structures can decay after a finite lifetime, the convective state once initiated remains sustained in all our runs.

Conditionally unstable convection is also highly sensitive to the aspect ratio. For small aspect ratios of 4 to 8, convection exhibits a recharge–discharge cycle, with short intense outbursts separated

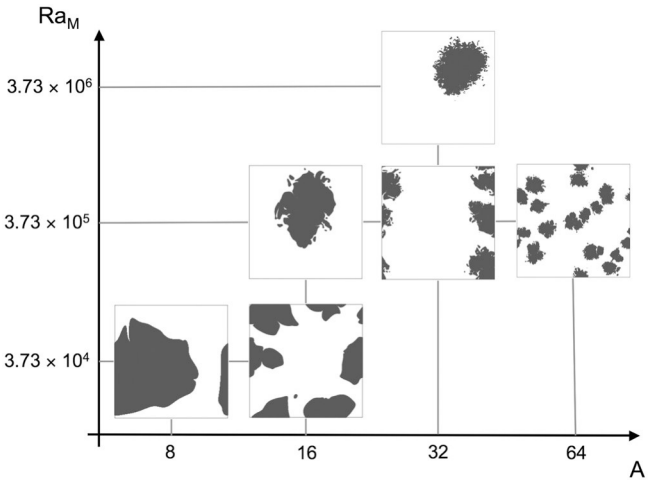

Fig. 6. Cloud cover as a function of the moist Rayleigh number and aspect ratio. Dark areas display clouds. The view is from the top onto the layer. A typical snapshot for each parameter set is shown.

by long phases of recovery. Convection in larger aspect ratio cells (at least 12 for the present parameters) exhibits a turbulent regime characterized by self-aggregation of moist convection in isolated cloudy patches embedded in an unsaturated and mostly quiescent environment. For this self-aggregated case, the vertical mean profiles of D and M differ only slightly from the linear conduction profiles, which indicates that molecular diffusion is active throughout the entire layer. We speculate that this behavior should persist even at high Rayleigh number, which should imply a finite upper bound on the Nusselt number (Eq. **17**).

A fundamental question is to which extent can our model provide insights on the dynamics of atmospheric convection. Indeed, it is highly idealized and omits key physical processes such as radiation and precipitation, while also introducing a rigid upper boundary. On the one hand, our study shows that although these processes are important for the dynamics of moist convection in the Earth atmosphere, they are not necessary to maintain self-sustained conditionally unstable convection. On the other hand, our simulations exhibit a strong dependency on diffusion, with significant diffusive transport through a large portion of the layer. It is unlikely that molecular diffusion is as important for atmospheric convection, as radiation and precipitation, both of which are associated with energy and water fluxes that are significantly larger than those induced by molecular diffusion and act on time scales that are comparatively shorter than the diffusion time scale across the troposphere. Nevertheless, our results confirm that the maintenance of self-sustained conditionally unstable convection requires a thermodynamic forcing, resulting from either combination of radiation, diffusion, or precipitation, that is active through a large portion of the atmospheric layer. Finally, the self-aggregation observed in moist Rayleigh–Bénard convection is reminiscent of similar behavior observed in the transition to open-cell oceanic convection and in simulations (26) of deep moist convection and thus appears to be an intrinsic aspect of the dynamics of moist convection.

ACKNOWLEDGMENTS. We thank Friedrich Busse, Bruno Eckhardt, Andrew Majda, Juan-Pedro Mellado, Bjorn Stevens, and Thomas Weidauer for fruitful discussions. The supercomputations were carried out on a Blue Gene/P at the Jülich Supercomputing Centre (Germany) under Grant HIL02. The work is supported by the Heisenberg Program of the Deutsche Forschungsgemeinschaft (DFG), by DFG-Grant SCHU1410/5-1, and by the US National Science Foundation under Grant ATM-0545047.

1. Shaw RA (2003) Particle-turbulence interactions in atmospheric clouds. *Annu Rev Fluid Mech* 35:183–227.
2. Stevens B (2005) Atmospheric moist convection. *Annu Rev Earth Planet Sci* 33:605–643.
3. Solomon S, et al. (2007) *Climate Change 2007—The Physical Science Basis. Contribution of Working Group I to the Fourth Assessment Report of the Intergovernmental Panel on Climate Change* (Cambridge Univ Press, Cambridge, UK).
4. Heintzenberg J, Charlson RJ (2009) *Clouds in the Perturbed Climate System* (MIT Press, Cambridge, MA).
5. Bony S, Dufresne J-L (2005) Marine boundary layer clouds at the heart of tropical cloud feedback uncertainties in climate models. *Geophys Res Lett* 32:L20806.
6. Moeng C-H, et al. (2009) The tropical marine boundary layer under a deep convection system: A large-eddy simulation study. *J Adv Model Earth Sci* 1:16.
7. Satoh M, et al. (2008) Nonhydrostatic icosahedral atmospheric model (NICAM) for global cloud resolving simulations. *J Comput Phys* 227:3486–3514.
8. Mellado JP (2010) The evaporatively driven cloud-top mixing layer. *J Fluid Mech* 660:5–36.
9. Bretherton CS (1987) A theory for nonprecipitating moist convection between two parallel plates. Part I: Thermodynamics and "linear" solutions. *J Atmos Sci* 44:1809–1827.
10. Emanuel KA (1994) *Atmospheric Convection* (Oxford Univ Press, Oxford, UK).
11. Pauluis O, Schumacher J (2010) Idealized moist Rayleigh-Bénard convection with piecewise linear equation of state. *Commun Math Sci* 8:295–319.
12. Bjerknes J (1938) Saturated-adiabatic ascent of air through a dry-adiabatically descending environment. *Quart J R Met Soc* 64:325–330.
13. Kuo HI (1961) Convection in an conditionally unstable atmosphere. *Tellus* 13:441–459.
14. Bretherton CS (1988) A theory for nonprecipitating moist convection between two parallel plates. Part II: Nonlinear theory and cloud field organization. *J Atmos Sci* 45:2391–2415.
15. Eckhardt B, Schneider TM, Hof B, Westerweel J (2007) Turbulence transition in pipe flow. *Annu Rev Fluid Mech* 39:447–468.
16. Moxey D, Barkley D (2010) Distinct large-scale turbulent-laminar states in transitional pipe flow. *Proc Natl Acad Sci USA* 107:8091–8096.
17. Schumacher J, Pauluis O (2010) Buoyancy statistics in moist Rayleigh-Bénard convection. *J Fluid Mech* 648:509–519.
18. Weidauer T, Pauluis O, Schumacher J (2010) Cloud patterns and mixing properties in shallow moist Rayleigh-Bénard convection. *New J Phys* 12:105002, 10.1088/1367-2630/12/10/105002.
19. Ahlers G, Grossmann S, Lohse D (2009) Heat transfer and large scale dynamics in turbulent Rayleigh-Bénard convection. *Rev Mod Phys* 81:503–537.
20. Krishnamurti R (1995) Low-frequency oscillations in turbulent Rayleigh-Bénard convection: Laboratory experiments. *Fluid Dyn Res* 16:87–108.
21. Krishnamurti R (2000) Low-frequency oscillations in turbulent convection. *Ann N Y Acad Sci* 898:122–126.
22. Hegseth JJ, Andereck CD, Pomeau Y (1989) Spiral turbulence and phase dynamics. *Phys Rev Lett* 62:257–260.
23. Malkus WVR (1954) The heat transport and spectrum of thermal turbulence. *Proc R Soc Lond A Math Phys Sci* 225:196–212.
24. Busse FH (1969) On Howard's upper bound for heat transport by turbulent convection. *J Fluid Mech* 37:457–477.
25. Howard LN (1972) Bounds on flow quantities. *Annu Rev Fluid Mech* 4:473–494.
26. Bretherton CS, Blossey PN, Khairoutdinov M (2005) An energy-balance analysis of deep convective self-aggregation above uniform SST. *J Atmos Sci* 62:4273–4292.

Supporting Information

Pauluis and Schumacher 10.1073/pnas.1102339108

SI Text

Fig. S1 demonstrates the difference between conditionally unstable moist convection and so-called linearly unstable moist convection for which both buoyancy fields are unstably stratified in the equilibrium configuration. Although convection is space-filling for the latter, it is strongly localized in the former case. For Rayleigh numbers at comparable magnitude (see caption for details) the level of turbulence is found to be significantly reduced in a conditionally unstable case. Fig. S2 adds further information for both cases by a comparison of the turbulent kinetic energy and the mean buoyancy profile.

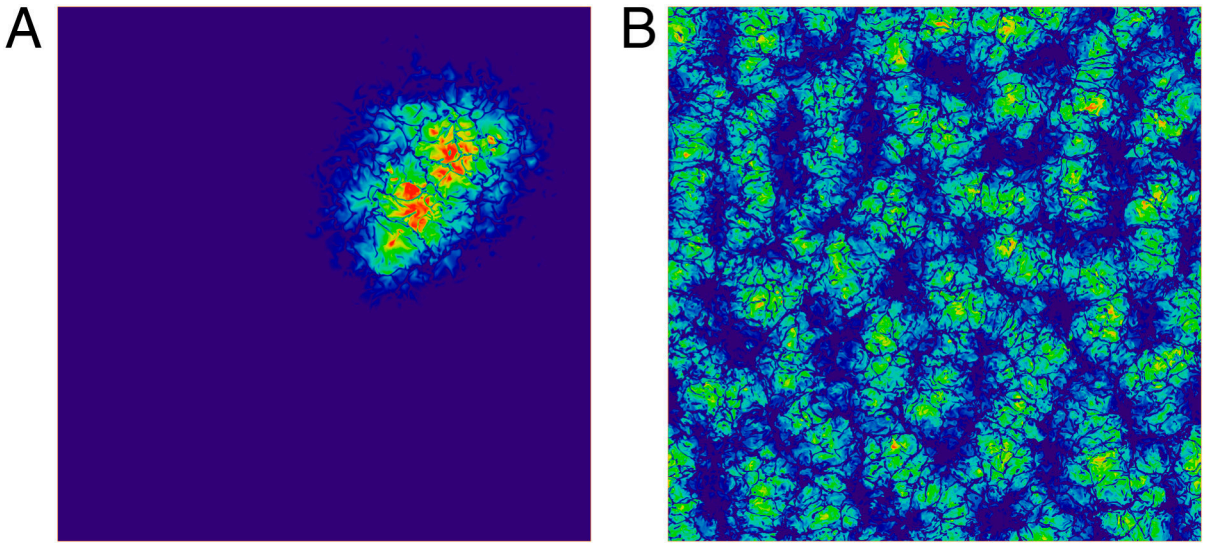

Fig. S1. Difference between moist convection in the conditionally unstable (*Left*) and the so-called linearly unstable (*Right*) regimes. The former is in the focus of the present work. The linearly unstable regime of moist convection is generated by exactly the same set of equations. Here, both the dry and the moist buoyancy fields, D and M, are unstably stratified. Instantaneous horizontal plane cuts through the rectangular simulation domain for the liquid water content $q_l(x,y,z_0,t_0)$ are shown. Contours starting with blue via cyan up to red are for concentrations of liquid water. Outside the cloud no water is existent (purple). Both simulations are for $A = 32$ and the computation is done for both cases on a $4{,}096 \times 4{,}096 \times 129$ grid. Conditionally unstable case: $Ra_M = 3.7 \times 10^6$, $Ra_D = -1.24 \times 10^6$, and $CW_0 = CW_H = 0$. Linearly unstable case: $Ra_M = 1.4 \times 10^7$, $Ra_D = 7.00 \times 10^6$, $CW_0 = 0$, and $CW_H = -0.43$. Data for the linearly unstable case are taken from ref. 1.

1. Weidauer T, Pauluis O, Schumacher J (2010) Cloud patterns and mixing properties in shallow moist Rayleigh-Bénard convection. *New J Phys* 12:105002.

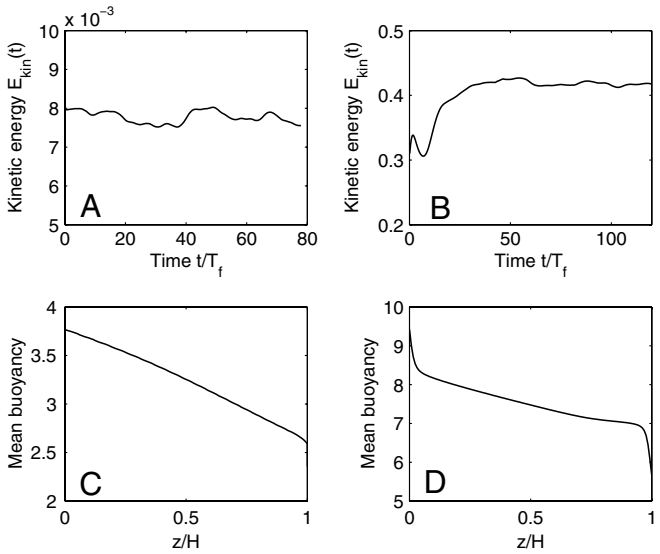

Fig. S2. Difference between moist convection in the conditionally unstable (*A* and *C*) and the linearly unstable (*B* and *D*) regimes. Data are the same as in Fig. S1. *A* and *B* display a time series of the turbulent kinetic energy. The turbulent velocity fluctuations in the conditionally unstable case are reduced by nearly two orders of magnitude. *C* and *D* show plane–time average of the buoyancy $\langle B(z) \rangle_{A,t}$ across the moist convection layer. *D* displays a well-mixed case with thin boundary layers at the top and bottom.